Journal of Solid State Chemistry 181 (2008) 1782–1791

Contents lists available at ScienceDirect

Journal of Solid State Chemistry

journal homepage: www.elsevier.com/locate/jssc

Structural study of ammonium metatungstate

Joel B. Christian [a,b,*], M. Stanley Whittingham [b]

[a] OSRAM SYLVANIA Global Tungsten and Powders, Towanda, PA 18848, USA
[b] SUNY at Binghamton, Materials Science Program, Binghamton, NY 13902, USA

ARTICLE INFO

Article history:
Received 12 December 2007
Received in revised form
14 March 2008
Accepted 24 March 2008
Available online 4 April 2008

Keywords:
Metatungstate
Polyoxometalate
Orientational ordering
Fuel cell catalyst

ABSTRACT

Several techniques have been used to study the structure of the Keggin-type polyoxometalate salt *ammonium metatungstate* (AMT)—$(NH_4)_6[H_2W_{12}O_{40}]^*nH_2O$, a potential fuel cell catalyst. The dehydrated salt is comprised of a mixture of crystallites of different unit cells in a centered eutactic cubic configuration, with an average unit cell of $a \cong 12.295$. Varied orientations of the Keggin ions in the cubic arrangement create the differences, and orientational variation within each unit cell size represents an energy well. Progressive hydration of each crystallite leads to expansion of the lattice, with the degree of expansion depending on the locations of the water added in relation to the Keggin ion, which is influenced by cation location and hydrogen bonding. The structural hypothesis is supported by *electron diffraction* of single and multicrystal samples, by powder density measurements, X-ray powder diffraction studies, synchrotron powder X-ray diffraction, and *a priori* structural modeling studies. Based on the structure, projected active site densities are compared with nanostructured platinum catalysts for fuel cell application.

1. Introduction

The title compound, ammonium metatungstate (AMT): $(NH_4)_6[H_2W_{12}O_{40}]^*nH_2O$ is a polycondensation product of solutions of ammonium tungstate. Also known as dodecatungstate, it is a Keggin-type polyoxometalate of the isopoly category; they are also known as heteropoly compounds, and in older literature as m-WO_3, hence the name metatungstate. The metatungstate ion has been widely used commercially for over 40 years, mainly as a precursor for preparing tungsten catalysts for hydrocracking [1] and de-NO_X [2] applications. The interesting redox properties of metatungstate have shown possible further applications in catalysis as a fuel cell catalyst [3–5]. The metatungstate ion and its unique solution properties are also a key to the technology of refining of tungsten from primary and secondary sources. The fuel cell catalyst application is particularly interesting, since structure properties are a key to understanding the performance and stability of a catalyst. Reduced metatungstate catalysts were shown to perform as hydrogen oxidation catalysts in a fuel cell setting [5]. The activation is believed to be caused by the electroreduction of tungstates and subsequent changes in spacing between the metal atoms [5,6]. The electrochemical transformation to a tungsten red, $(H_{24}[H_2W_{12}O_{40}])^{6-}$, creates an observed structural change similar to dehydration. A next step in catalyst development would be to study the solid state forms of metatungstate to determine if the required site density can be met with known forms.

1.1. PEM fuel cell interfaces

The proton exchange membrane fuel cell (PEM or PEMFC) operates by separating an anode and cathode by a proton exchange membrane. The membrane must be an excellent electrical insulator as well as an excellent proton conductor. Catalysts are placed on both sides of the membrane, and supplied with hydrogen and oxygen, respectively. Fig. 1 shows an idealized PEM cell section, with the proton path moving from left to right, showing graphite support, anode catalyst, membrane, cathode catalyst, and graphite support. Typical catalysts are platinum nanocrystals on a graphite support with Pt crystals about 37 Å in diameter [7]. Electrical power can be drawn from the two gas distributors.

1.2. Metatungstate background

AMT has a very high solubility, 1.6 kg L^{-1} at room temperature. The metatungstate ion, $[H_2W_{12}O_{40}]^{6-}$, is a polyoxometalate ion that forms in aqueous solutions of monotungstate upon pH adjustment. While the metatungstate salts formed from larger cations have been studied by single-crystal X-ray diffraction (XRD) studies, AMT forms a range of hydrates that are not suited to formation of single crystals. Characterizing AMT powders by

* Corresponding author at: OSRAM SYLVANIA Global Tungsten and Powders, Towanda, PA 18848, USA. Fax: +1 570 268 5350.
E-mail address: joel.christian@sylvania.com (J.B. Christian).

0022-4596/$ - see front matter © 2008 Elsevier Inc. All rights reserved.
doi:10.1016/j.jssc.2008.03.034

powder XRD can be frustrating since XRD patterns often vary, due in major part to the change in water content [8]. Phase identification can be difficult since only one AMT powder diffraction file is in the ICDD-JCPDS database [9].

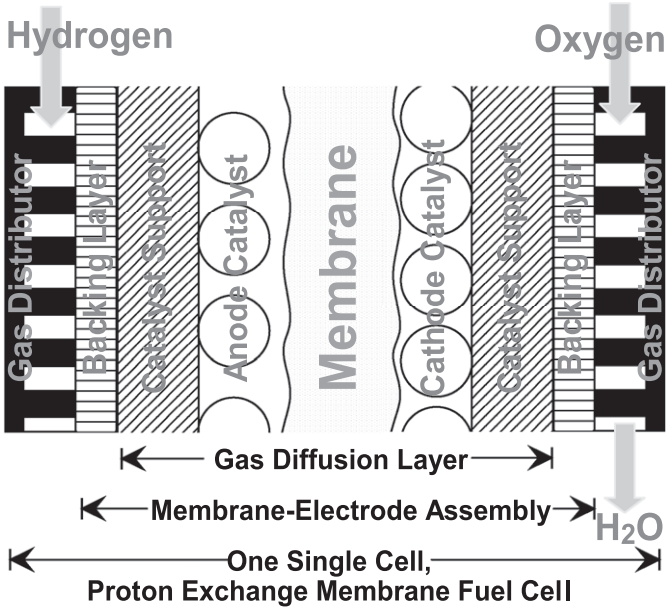

Fig. 1. Schematic cross-section of a fuel cell showing the sequential path for protons from left to right through one complete cell. Various commonly used terms and acronyms are shown including the gas-diffusion layer (GDL), membrane-electrode assembly (MEA), and proton-exchange membrane fuel cell (PEM or PEMFC).

The compounds studied are detailed in Table 1. This study builds on work done in this lab 45 years ago when the commercial process was originally developed by Mooney et al. [8], whose work showed that water content varied the structure, and that zeolitic water may account for the structural changes. Mooney et al. identified five hydrates, denoted AMT-0, AMT-1, AMT2–6, AMT12–15, and AMT20–22, with the numbers denoting the number of waters contained. Each was identified by Mooney with major XRD peaks and by gravimetric measurements. Relating to other Keggin ions, the metatungstate ion has a high ionic charge (6−) and also the most stable upon electroreduction [10], which suggests that electron density is higher in the terminal oxygens than in other Keggin ions. In comparison, phosphotungstate $[PW_{12}O_{40}]^{3-}$ [11] and the molybdenum analog $[PMo_{12}O_{40}]^{3-}$ [12] have been studied extensively and structures have been determined. Higher charged Keggins $[SiW_{12}O_{40}]^{4-}$, $[FeW_{12}O_{40}]^{5-}$, and also $[CoW_{12}O_{40}]^{6-}$ as well as metatungstate have undergone successful structural determinations, especially noted here in high-density forms that involve tighter packing. A summary appears in Table 2. Table 2 includes both density and cell volume per Keggin, the latter which better compares molybdate with tungstate Keggin structures. The $[PMo_{12}O_{40}]^{3-}$ ion was shown by Boeyens et al. [12] to move from primitive cubic with $z = 8$ to centered cubic with $z = 2$ as dehydration proceeds, similar to our findings for AMT. Mao et al. [11] has shown in structure determinations from powder diffraction that $[PW_{12}O_{40}]^{3-}$ is a structural analog to $[PMo_{12}O_{40}]^{3-}$ and exhibits a very high powder density.

1.3. Prior structural information

Structure determination is aided in part by supplementary prior information. The Keggin structure was first determined by Keggin in 1934 [13]. While slight variations in size exist, the ion is

Table 1
Crystal data and structure summary for compounds 1 through 4

Compounds	**1**	**2**	**3**	**4**
Formula	$(NH_4)_6[H_2W_{12}O_{40}]$	$(NH_4)_6[H_2W_{12}O_{40}]^*H_2O$	$(NH_4)_6[H_2W_{12}O_{40}]^*4H_2O$	$(NH_4)_6[H_2W_{12}O_{40}]^*{\sim}20H_2O$
Formula weight	2956.2	2974.2	3028.3	3334.2
Temperature (K)	293	293	293	293
Crystal system	Cubic	Cubic	Not determined	Distorted cubic
a (Å)	12.295	12.68	13.11	~17.89
V (Å^3)	1854	2038	2253	5727
Z	2	2	2	4
$\rho_{measured}$ (g/cm^3)	5.293	4.860 (*est.*)	4.455	3.867 (*est.*)
V/Z (Å^3/Keggin)	927	1016	1127	1432
Mooney designation [8]	AMT-0	AMT-1	AMT2–6	AMT20–22
nH$_2$O	0	1 (est)	4.0	20 (est)

Table 2
Keggin ion packing density studies

n	Author	Compound	Space group	Density (g/cm^3)	V/z (Å^3/Keggin)
1	This study	$(NH_4)_6[H_2W_{12}O_{40}]$	Distorted cubic	5.293	927
2	This study	$(NH_4)_6[H_2W_{12}O_{40}]^*4H_2O$	Distorted cubic	4.455	1127
3	This study	$(NH_4)_6[H_2W_{12}O_{40}]^*(20\text{-}22)H_2O$	Distorted cubic	3.867	1432
4	Jeannin et al. [14]	$Rb_4\ H_2\ [H_2W_{12}O_{40}]^*18H_2O$	Cubic	4.356	1341
5	Zavalij et al. [23]	$[NH_2(CH_3)_2]_6\ [H_2W_{12}O_{40}]^*4H_2O$	Orthorhombic	3.47	1429
6	Zavalij et al. [23]	$[N(CH_3)_4]_6[H_2W_{12}O_{40}]^*2H_2O$	Orthorhombic	3.534	1563
7	Asami et al. [24]	$[(CH_3)_4N]_6[H_2W_{12}O_{40}]^*9H_2O$	Monoclinic	3.09	1861
8	Yamase and Ishikawa [15]	$K_6\ [BW_{12}O_{40}]^*13.5H_2O$	Triclinic	4.599	1180
9	Gabriel et al. [25]	$[H_3N(CH_2)_6NH_3][PMo_{4.27}W_{7.73}O_{40}]$	Monoclinic	3.55	1323
10	Lee et al. [26]	$(CH_6N_3)_8[\alpha\text{-}SiPt_2W_{10}O_{40}]^*6H_2O$	Tetragonal	3.464	1671
11	Weiner et al. [22]	$[FeNiW_{11}O_{40}]$	Cubic	3.843	1406
12	Han et al. [27]	$K_2NaH[GeW_{12}O_{40}]^*7H_2O$	Hexagonal	3.973	1316
13	Mao et al. [11]	$Rb_3[PO_4W_{12}O_{36}]$	Cubic	6.563	792

fairly fixed in structure, a metal oxide with four trigonal caps of edge-shared MO_6 groups (M = Mo, W, Ta, Nb, V), corner-shared to form a roughly spherical cubooctahedron structure when considering the metal atoms. Various fully oxidized and partially reduced Keggins have been studied. The size and orientation of the oxygen atoms fixes the outer size. Reduction of the metals in the MO_6 groups has been shown to relocate the metals within the octahedra to balance the charge [14,15], which is believed to give rise to catalytic activity for hydrogen oxidation [5,6]. We also noted that the powder XRD pattern of AMT of the activated catalyst (Ref. [5], Fig. 1E–G) followed a very similar transition to that observed for dehydration (Fig. 3). This suggests that the catalyst activation step may be physically similar to dehydration, thus the study of rearrangement during dehydration, combined with electroreduction, forms a more complete description of the catalyst system. Recent kinetic studies confirm that the electroreduction of metatungstate results from coupled reactions [6,16] with protons stabilizing the reduced metals without a loss of the Keggin structure. It would make sense that tighter-packed crystals of Keggin structures would be more conductive by reducing proximity between Keggin ions. While the Keggin ions would be conductive internally, closer proximity to neighboring ions should make a more conductive crystal for electrocatalytic applications. Table 2 summarizes key structure determinations in the literature for comparison. The dense structures tend to be cubic, where structures with larger and less polar cations tend to form more orthorhombic or monoclinic forms, with lower powder density and larger spacings between Keggin ions.

2. Experimental

2.1. Preparation of materials

Commercial AMT was used (OSRAM SYLVANIA, Catalyst Grade) for all experiments. It was used as-is and also from a stock solution, dissolved at 1.6 kg of salt per 1 L of water. All solutions were handled exclusively in plasticware to prevent formation of silicotungstates (e.g. $[SiW_{12}O_{40}]^{4-}$). Aqueous ^{183}W NMR was performed on the as-received material dissolved in D_2O, which gave one single-frequency shift peak at −115.2 ppm, against a standard of Na_2WO_4 in D_2O; consistent with a tungsten Keggin structure. Single crystals of $(NH_4)_6[H_2W_{12}O_{40}]$*20–22$H_2O$ (AMT20–22) were grown from this stock solution. Crystals were allowed to grow slowly from the stock solution. The crystals that formed had many faces of varied size, no obvious crystal habit could be deduced from their shape. Crystals of the ~20 water hydrate must be stored in the mother liquor. Crystals exposed to air begin drying immediately to form the ~4 hydrate form, which is a fine powder. Recrystallized samples were prepared from ~20 water hydrate crystals in this way, with light grinding with a ceramic mortar and pestle, and dried to AMT-0. The ~0 water hydrate form was also prepared from ~4 water hydrate, fired in air at 200 °C for 5 days. Samples dried to 150 °C were prepared in a similar fashion. Diffractograms of fired samples were run immediately after removal from the furnace. Diffractograms were identical for AMT-0 produced from as-received AMT2–6 and from AMT20–22 crystals. Samples that were dried to 150 or 200 °C were also re-dissolved at 1.6 kg of salt per L of water to confirm that the highly soluble Keggin structure remained intact. The 150 and 200 °C samples were also fired to WO_3 in air at 650 °C and a gravimetric determination confirmed that the AMT was fully dehydrated. Thus, both the 150 and 200 °C dried materials were fully soluble and fully dehydrated, and the structure was independent of synthesis path. The as-received material had a measured hydration n of 4.02, hereinafter referred to as AMT-4. Pycnometer tests were performed on as-received, 150 and 200 °C materials. These test results are summarized in Table 1. SEM imaging of the as-received material show hollow spheres characteristic of spray-dried powders. Single-crystal XRD of grown AMT20–22 crystals was attempted, but disorder from Keggin locations and water prevented a definitive structure solution.

2.2. Characterization

Density measurements were performed with a pycnometer with a sample size of approximately 5 g. XRD patterns were obtained with a *Rigaku Geigerflex* diffractometer using a Cu$K\alpha$ X-ray beam and measured at ambient temperature. Furnace-XRD patterns were measured with a *Philips X'pert MPD*. Synchrotron powder diffraction was performed at the Cornell High Energy Synchrotron Source (CHESS) station B2, with $\lambda = 0.4959$ Å. A high-pressure diamond anvil was used as the sample holder. A cerium oxide standard was used for calibration. Electron diffraction patterns (TEM-ED) were obtained with a *Hitachi H-7000* TEM at 100 kV. An aluminum metal standard was used for determining the camera constant for each session. Camera lengths of 0.8 and 1.6 m were used. AMT powder samples were dissolved in water on the surface of a copper-formvar TEM grid, then dried in an oven at 60 °C for 10 min, or 115 °C for 15 or 60 min, yielding a sample where $n H_2O$ is in the range $0 \leqslant n \leqslant 1$.

2.3. Structure solution

Structure fitting calculations were performed with the "*Endeavour*" software package, published by Crystal Impact, version 1.4 (www.crystalimpact.com). *Endeavour* employs a Monte Carlo structure solution methodology, and includes fitting to potential energy (PE) as well as to diffraction patterns, and weighed combinations of the two, which create a cost function which can be minimized [17]. The combination of both of these methods proved to be more useful in our case. *Endeavour* can use "molecules" as well as atoms in structural fitting. A "molecule" approach was used, using the Keggin anion as the "molecule". The Keggin molecule definition was derived from the data of Jeannin et al. [14], who formed the hydrated Rb salt of metatungstate. Only the W(VI) locations of Jeannin et al. were used for this study, the reduced W(IV) locations were ignored in the molecule definition for this work. Other molecule definitions were also tried with no appreciable difference. The input parameters were set to fix one Keggin centered at (0,0,0) with rotation allowed, and to place one Keggin centered at $(\frac{1}{2},\frac{1}{2},\frac{1}{2})$ with rotation and relocation allowed to make up for changes in symmetry between the two ions. Particular importance was placed on fitting to the peaks that appeared in both the TEM-ED and the XRD data. The input files and structure solutions for Fig. 7e–l are available in a *crystallographic information file* (CIF) which can be accessed at the *Predicted Crystallography Open Database* (PCOD) at www.crystallography.net.

3. Results

3.1. Synchrotron indexing

Synchrotron XRD of the as-received powder shows a unique pattern, as seen in Fig. 2a. This material was dried for 8 days at 150 °C to consolidate the structure. Synchrotron XRD of a freshly prepared sample dried at 150 °C (Fig. 2b), shows a smaller unit cell

with greatly improved definition. The dried material was indexed as a cubic structure as shown in Fig. 2c. This figure shows a very clean XRD pattern with well-defined peaks, showing systematic absences consistent with a BCC structure, with $a = 12.8175$. The inset graph shows the magnified peaks at smaller d values, and the image of the raw data shows a strong signal for the first three main peaks.

3.2. XRD patterns

Powder XRD patterns were obtained for the as-received AMT2–6, samples dehydrated at 150 °C and dehydrated at 200 °C. Typical drying batches were 50 g, dried for about 8 days in air. Powder XRD patterns were also obtained with a furnace accessory to see the temperature effects in situ. A summary of results is shown in Fig. 3. Beginning at the bottom are as-received raw material, $(NH_4)_6[H_2W_{12}O_{40}]^*4H_2O$, that material dried in air for 1 day at 200 °C, then dried 5 days at 200 °C, then partially exposed to air and moisture prior to running a temperature series with a furnace accessory.

Fig. 3 shows the clear structural simplification after drying the as-received material. The dried material that is again exposed to air shows at least three main peaks at 9–10° that upon progressive drying simplifies to one peak again. Figs. 3b and c are bulk dried samples, with a batch size of about 50 g, Fig. 3d–h are a thin layer glued to an aluminum support for furnace XRD. The dried material in Fig. 3b shows a broad peak at 9–10° that becomes sharper after 5 days of drying (Fig. 3c).

3.3. TEM-ED

The selected area diffraction method was used for TEM-ED analysis. Aluminum standards were used for calibration. Ring diameter D was measured from the film, and ASTM d values of Al were used for calculation of camera constant, K. TEM grids were prepared that featured many crystals, so several measurements could be made on one identically prepared sample platform. Fig. 4 shows representative TEM-ED patterns, which are cross-referenced in Table 3. On analysis of the data, many slightly different a parameters were found, forming a statistical distribution similar

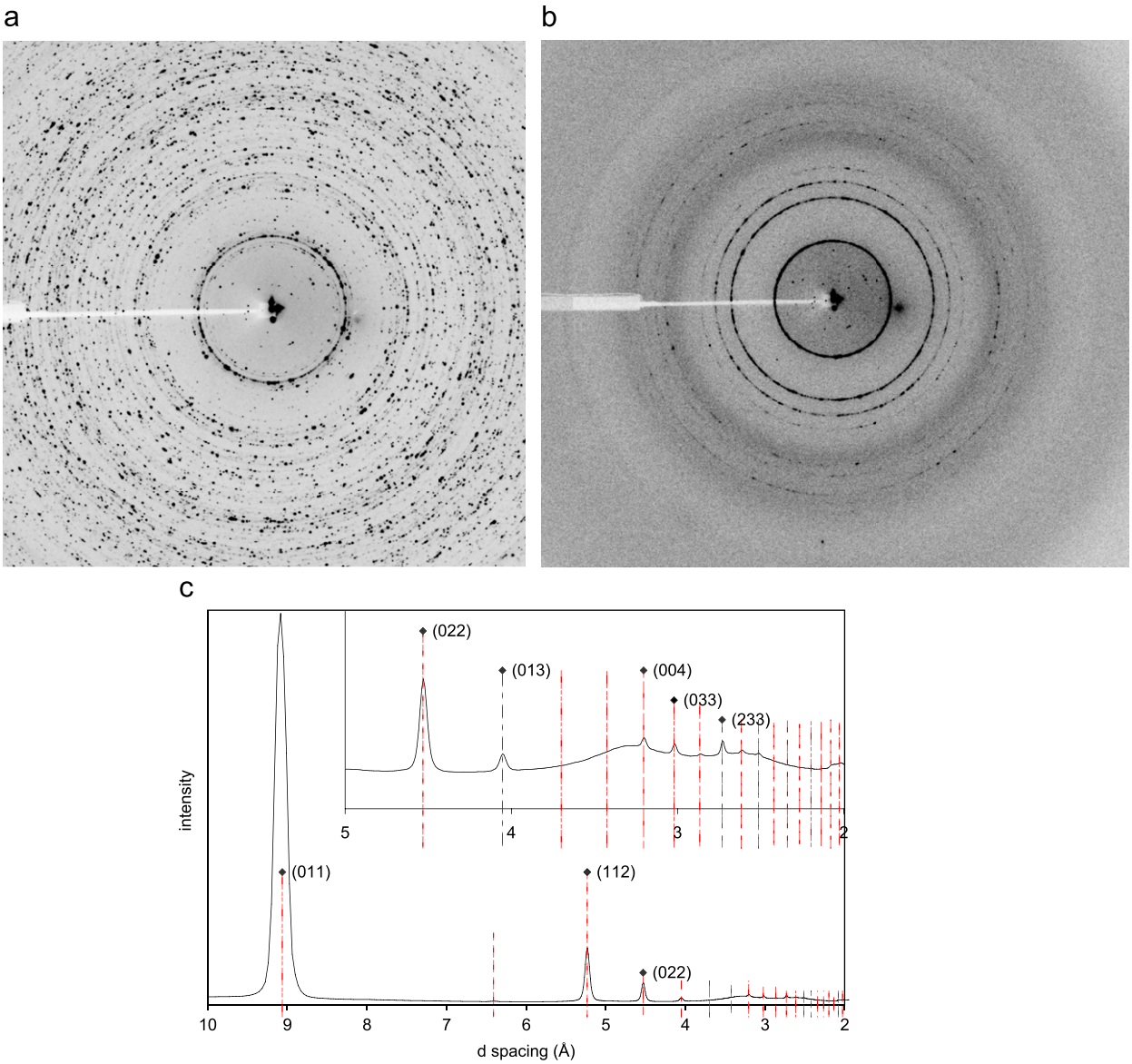

Fig. 2. Synchrotron XRD pattern of AMT dried at 150 °C: (a) as-received (before drying), (b) dried sample, and (c) dried sample, integrated plot. Major BCC crystallographic peaks are identified.

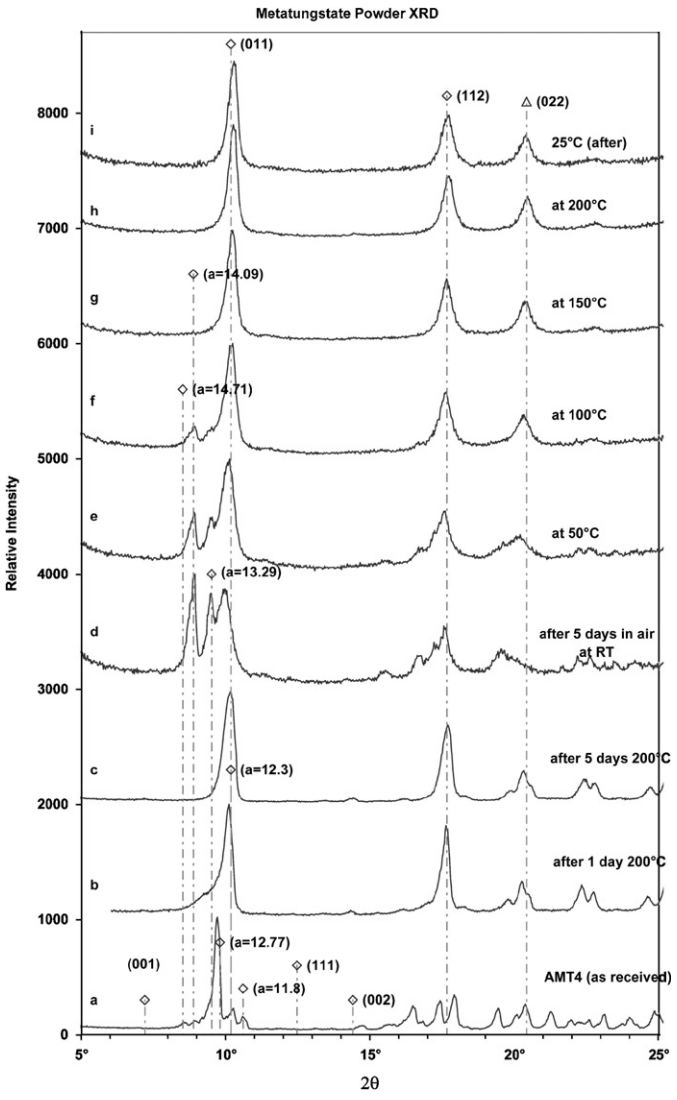

Fig. 3. Experimental XRD patterns. From the bottom: as-received, dried 1 day, dried 5 days, exposed to air, then furnace series RT to 200 °C and final RT.

to the powder XRD pattern, as shown in Fig. 5, which plots a histogram of TEM-ED data under the bulk powder XRD pattern. Note that the peak shapes are very similar comparing the powder XRD and the TEM-ED histogram. Table 3 shows various measured a parameters from TEM plates and estimates of a by other methods. Fig. 5 (inset) shows the variation of the TEM-ED d measurements in sequence, against the median and 2σ bars of the TEM-ED data set. Also shown as a dashed line is the average of non-TEM methods (XRD and density) showing their agreement. The slight shift in central tendency of the TEM-ED values vs. XRD at ~8.7 Å may be due to the shorter crystal drying time for TEM samples, and also to variation in determining the camera constant. Even with systematic errors common to TEM-ED measurements [18], the general trend for variation in a parameter remains valid.

3.4. Indexing and structure fitting

For TEM and synchrotron samples (Figs. 4 and 2), patterns indexed to body-centered cubic (BCC), with varied a parameters. For bulk laboratory powders, indexing patterns including all peak positions with *McMaille* [19] provided very few plausible unit cells, and no definitive fit. Likely proposals were run in *Endeavour* for 11 trials to check for a fit to the powder data, with only the BCC structure providing any realistic fit to the data.

Indexing and structure fitting found, in general, a pseudo-BCC-type arrangement of Keggins, with one Keggin structure located at (0,0,0) and one Keggin located at or near $(\frac{1}{2},\frac{1}{2},\frac{1}{2})$. For pattern fitting, a central "dummy" atom of helium or hydrogen was added to the molecule definition to locate the Keggin ion's center, in lieu of the two protons that occupy the tetrahedral position in the center. The BCC-type arrangement gives a very strong peak in the 8–11° 2θ range, which is characteristic of all the materials studied as well as of past studies [8]. The scattering of the two central hydrogen atoms was not discernable in the powder pattern. Likewise, the location of the NH_4^+ cations and water were dwarfed by the strong geometry of the metatungstate ion, so the locations of the cations were not determined in this study. Further structure modeling has shown a limited but connected void space that allows for mobility of cations and water. The cations are likely to be

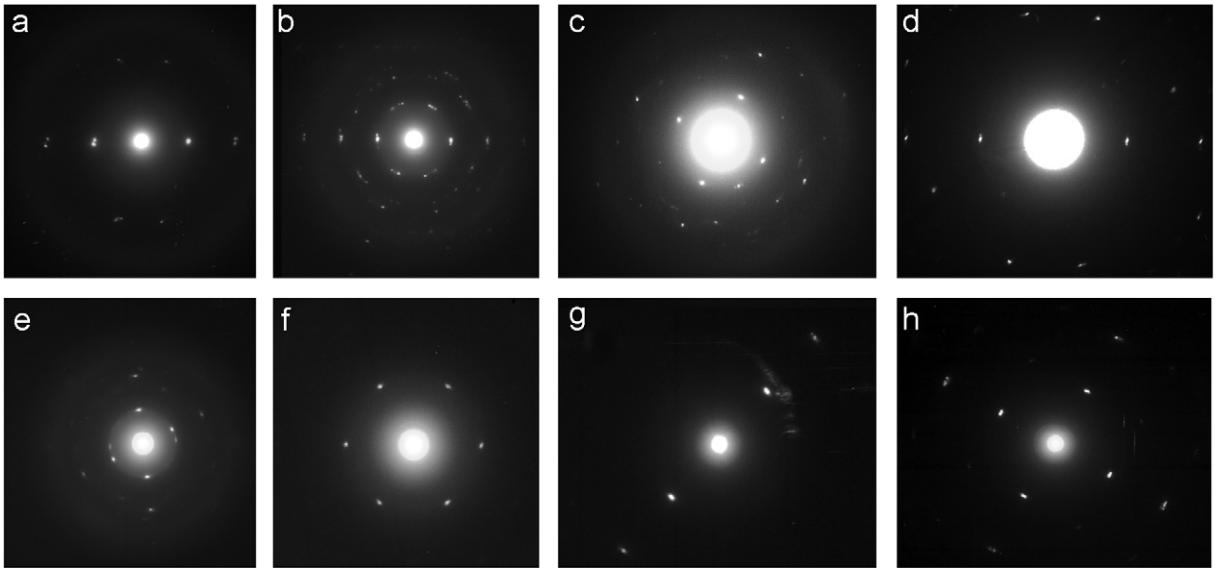

Fig. 4. TEM-ED patterns (identified in Table 3).

Table 3
Comparison of *a* by TEM-ED and other methods

Type	n_{TEM}	ID	Crystal type	*a*	*d*	Drying
ED	1	Plate 6346	Single	11.906	8.419	60 °C, 10 min
ED	2	Plate 6349	Multi	12.331	8.720	60 °C, 10 min
ED (Fig. 4a)	3	Plate 6351	Multi	11.906	8.419	60 °C, 10 min
ED (Fig. 4b)	4	Plate 6352	Multi	12.331	8.720	60 °C, 10 min
ED (Fig. 4c)	5	Plate 7088	Single	12.115	8.567	60 °C, 10 min
ED	6	Plate 7090	Single	11.906	8.419	60 °C, 10 min
ED	7	Plate 7128	Single	12.674	8.962	60 °C, 10 min
ED (Fig. 4d)	8	Plate 7130	Single	12.553	8.876	60 °C, 10 min
ED	9	Plate 7384	Single	12.681	8.967	115 °C, 10 min
ED (Fig. 4(h)	10	Plate 7385	Single	12.633	8.933	115 °C, 10 min
ED	11	Plate 7387	Single	12.466	8.815	115 °C, 60 min
ED (Fig. 4(g)	12	Plate 7388	Single	12.498	8.837	115 °C, 60 min
ED (Fig. 4e)	13	Plate 7389	Twin	12.903	9.124	115 °C, 60 min
ED	14	Plate 7390	Single	12.903	9.124	115 °C, 60 min
ED	15	Plate 7391	Single	12.791	9.045	115 °C, 60 min
ED (Fig. 4f)	16	Plate 7392	Single	12.537	8.865	115 °C, 60 min
Synchrotron		CHESS s1	Compressed powder	12.817	9.063	150 °C for 5 days
XRD		150C 8d	Powder	12.365	8.743	150 °C for 8 days
XRD		200C 5d	Powder	12.295	8.694	200 °C for 5 days
Density		150C 8d	Powder	12.319	8.711	150 °C for 8 days
Density		200C 5d	Powder	12.284	8.686	200 °C for 5 days
XRD		Mooney [8]	Powder	12.304	8.7	AMT-0 (⩾115 °C)

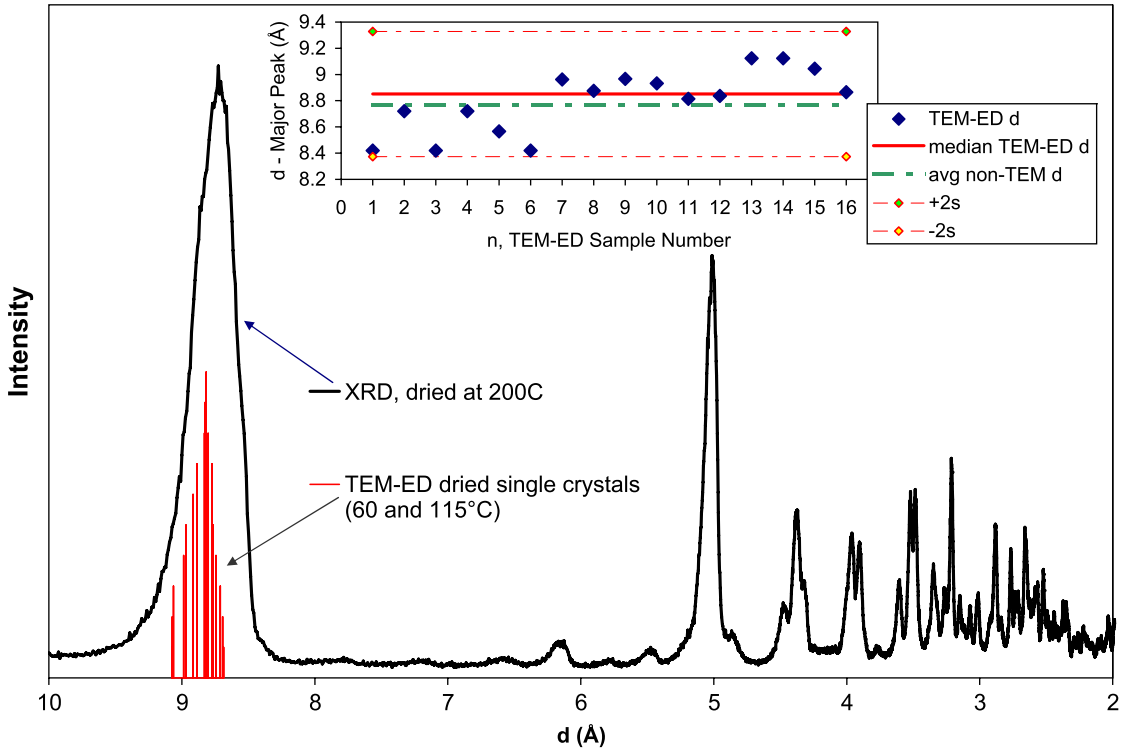

Fig. 5. Comparison of laboratory XRD and TEM-ED. Laboratory bulk powder XRD pattern shows large peaks at 8.7 and 5 Å. TEM-ED (below curve) shown as a histogram of $d_{(max)}$ values from 16 individual measurements. Inset: TEM-ED distribution of individual $d_{(max)}$ values (diamonds), median of TEM-ED values (solid line) and average of bulk measurements of $d_{(max)}$ calculated from pycnometer density and powder XRD (dashed line).

mobile, occupying any number of locations within the eutectic framework.

A structure fit was performed using *Endeavour* software to verify the observed XRD pattern. The AMT-0 pattern was used for structure fitting. *R* values as low as 5% were obtained through simulated annealing with several impurity peaks removed. Fig. 6 shows the proposed structure, and Fig. 7d shows the calculated XRD data. For the crystals of AMT20–22, a preliminary XRD pattern was generated from single-crystal XRD of the prepared crystals of AMT20–22, the calculated pattern is shown in Fig. 7c.

3.5. *A priori* simulations and calculated XRDs

Next, to frame the structural characteristics of various unit cell sizes, a $z = 2$ Keggin cell was simulated at various BCC unit cell

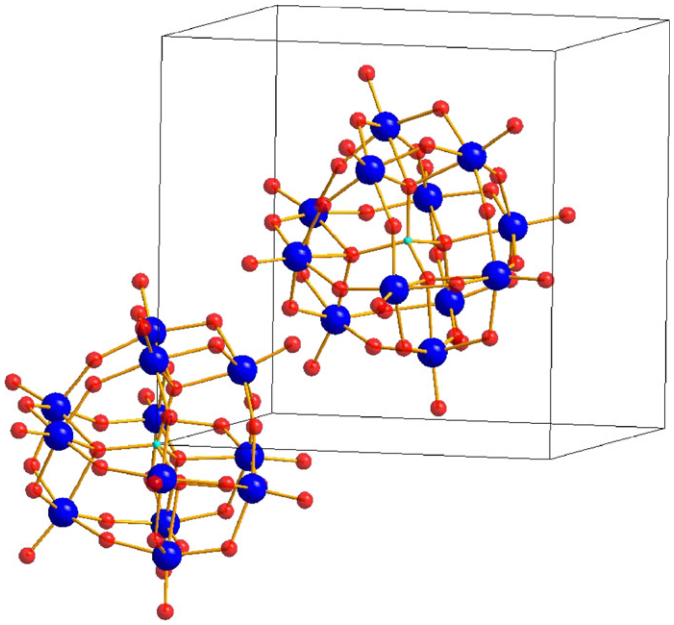

Fig. 6. Structure Fit for AMT-0. Molecule 1 is fixed at (0,0,0) for the structure solution, but molecule 2 is located at (0.4860, 0.5119, 0.4730), illustrating the displacement from strict BCC locations due to molecular interaction and allowed space conditions.

sizes. Fig. 7 shows the results of these *a priori* tests. From this plot, it is clear that smaller cell sizes give many even-sized peaks, whereas larger cells have one large initial peak, followed by many peaks that are much smaller. These simulations agree with the experimental patterns, and this comparison is especially useful for identifying larger cells, as indexed by both XRD and pycnometer density. For example, the pattern for the structure of Mao et al. resembles the Fig. 7e pattern at $a = 11.666$. Also, the high-pressure pattern shown in Fig. 2c, resembles the plot at $a = 13.11$. In this way, the measures of peak height ratios may be more useful for structure identification than the actual peak positions, owing to measurement error and structural variability. This structural variability is illustrated in Fig. 5, where the histogram of TEM-measured sizes fit within the broad powder XRD peak at about 9 Å.

4. Discussion

Structure simulation gives insight into the general structure and long-range order of the four main forms, moving towards a general model for all four forms. The dehydrated form, AMT-0, varies based on anion rotation effects (orientational ordering). The hydrated forms, AMT-1 to AMT20–22, likely rely on structural water (hydrogen bonding) to expand the lattice, further complicated by orientational ordering.

Given the known high purity of the sample, the "impurity" (non-indexed) peaks observed should originate from structural phenomenon rather than impurities. The TEM data suggest that dried powders consist of a mixture of similarly sized crystallites, which would account for peak broadening at low 2θ values, and a high number of "impurity" peaks at higher 2θ values. In this way, the bulk powder XRD pattern represents the average of a mixture of similar d values at larger experimentally observed d values. This is illustrated in the large peak in Fig. 5. Synchrotron and TEM-ED experiments, which use smaller samples, gave very clean eutactic-BCC structure patterns. Molecule rotation disorder and molecule displacement can explain the different sizes observed, as well as the large number of peaks appearing in the 2–4.5 Å range in Fig. 5.

For simplicity, this discussion will assume unit cell expansion creates BCC cells. Single-crystal studies (Table 2) show that cubic structures distort to more complicated structures, such as centered tetragonal, although those studies typically employ large hydrophobic cations that aid crystallization but also elongate the structure from simple cubic due to cation geometry. For small cations and large anions, the BCC assumption is a reasonable starting point for compounds 1–3.

4.1. Rotational disorder

Rotational disorder (orientational ordering) is well-known for C_{60}, "Buckyballs" [20]. Buckyballs have no charge, so the rotational effects do not impart a structural effect as they would with AMT. Also, they are more symmetrical about the axis, so axis errors are not expected. The effects of cations and hydrogen bonding are also absent in pure C_{60}. Finally, since they are spheres not cubes, the rotational displacements illustrated in Fig. 8 would not occur. Considering metatungstate structures with a less spherical molecule, hydrogen bonding, and final cation location possibilities all combine to make the structure of AMT much more complex.

Rotational disorder observed in modeling was due to orientational possibilities (not to free rotation). Structure models show that Keggin ions are fixed for AMT-0, contrasted with AMT20–22, which could have mobility and free rotation for all components. This rotational effect appears in three ways: the rotation of the Keggin during consolidation, displacements due to the location of the cation and templating water, and the geometric effect of 12-sided molecules occupying a site with eight neighbors. The rotational effect is illustrated in Fig. 8, which shows the orientation effect using strict (0,0,0) and $(\frac{1}{2},\frac{1}{2},\frac{1}{2})$ locations. This structure fit used four adjacent BCC unit cells, fitting to XRD data through 21° 2θ and minimizing PE at a 50/50 weight. The Keggin molecule definition includes 12W atoms, the first position, W1, is shown as red polyhedra in each Keggin. After simulated annealing, the W1 position is different in every anion. This positioning effect is expected throughout the crystal, making long-range order prominent in bulk XRD patterns, while randomizing and confounding short-range order data at higher vales of 2θ. This mix of long- and short-range order can be seen in the synchrotron images in Fig. 2. Whereas the hydrated salt in Fig. 2a has many sharp point images throughout the range, the dehydrated salt shows increased order for the first 3 to 4 rings, then a large gray ring with few visible points in the 2–4 Å range.

4.2. Hydration and structural water

The effects of hydration and structural water were also studied via simulation, which yielded a blend of pinning structural waters and free zeolitic waters, summarized in Table 4 and illustrated in Fig. 9. Pinning structural waters likely attach to Keggin ion sites during consolidation via hydrogen bonding. Hydration tends to separate the Keggin ions, which would help explain why hydrated forms did not show catalytic activity during activity testing.

The combined structural variation of rotation, displacement, and hydration are illustrated in two dimensions in Fig. 10, using a cubic grid, with individual Keggins shown as octagons, their X-ray scattering centers shown within as white circles, and hydrating waters as spheres. The highest structural order is shown in the lower left in each case, progressing in disorder effects moving to the upper right, with lines added showing the apparent unit cell size and disorder resulting from the arrangements.

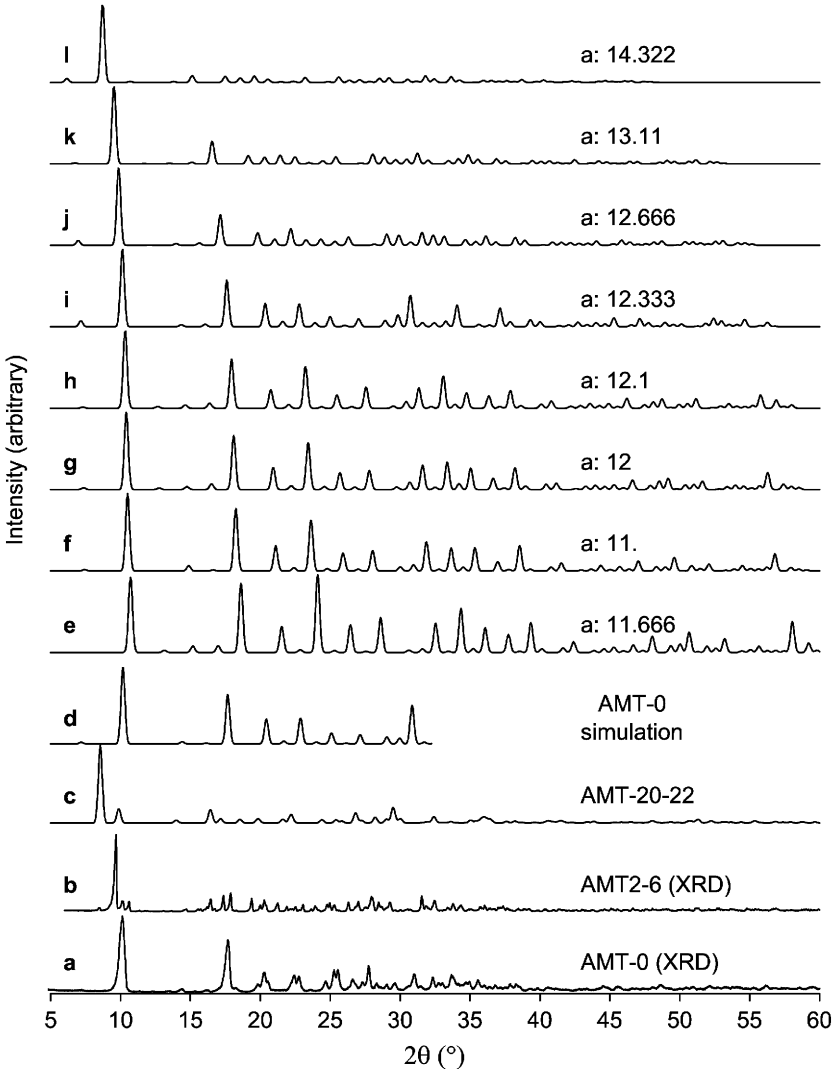

Fig. 7. Comparison of simulated and actual XRD patterns: (a–c) actual data, (d) structure fit to data, (e–l) *a priori* simulations based on energy minimization, (e) represents the smallest documented tungsten Keggin packing [11], (l) represents the largest dimension observed (for AMT20-22). *A priori* simulations based on a cubic cell , illustrate a trend in ratios of relative peak height from $d_{(max)}$ to the next three major peaks from 1:1 to about 20:1 as the cell expands.

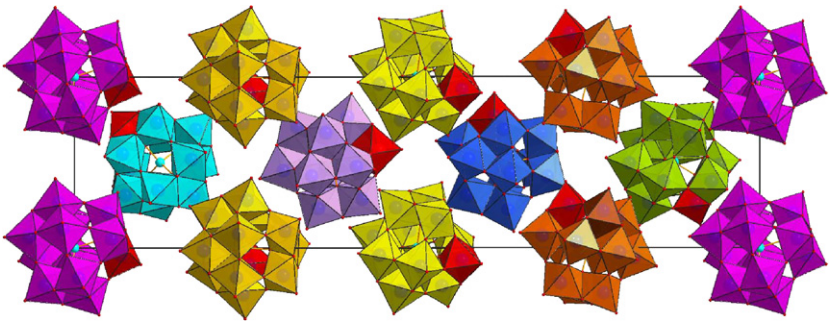

Fig. 8. 4 × AMT supercell simulation showing rotational disorder. Each independent molecule is shown in a different color. Red polyhedra mark W1 positions. Molecule centers in this view are fixed at (0,0,0) and $(\frac{1}{2},\frac{1}{2},\frac{1}{2})$ for simplicity.

4.3. Catalyst considerations

After this modeling study, the powder XRD pattern similarity between the dehydrated AMT (Fig. 5) and the electrochemically activated AMT catalyst (Ref. [6], Fig. 1E) indicate that these same compact interlocking assemblies of Keggins seem to be required for catalytic activity. These assemblies were formed by aqueous electroreduction to a red metatungstate [5,6] and by dehydration (*this study*). Since only surface W–W–W sites are expected to be active, control of the crystal size would be a logical next step.

Active sites could be thought to mimic the surface geometry of platinum surfaces. Fig. 11 compares these. Fig. 11a shows a typical Pt nanocrystal, based on HRTEM work presented by Ross [7]. Figs. 11b and c show metal triplet sites, suitable as three-fold

Table 4
Comparison of ammonium metatungstates, simplified to cubic, $z = 2$

Mooney class	a	ρ (g/cm^3)	d at $I_{(max)}$ (Å) [6]	Structure summary
AMT22–24	14.7	3.73	10.4	6 pinning H_2O/Keggin, zeolitic water crowded
AMT12–15	14.39	4.20	10.7	6 pinning H_2O/Keggin, 6–9 zeolitic waters
AMT2–6	13.11 (from ρ)	4.45	9.3	~3 pinning H_2O/Keggin 0–3 zeolitic waters
AMT-1	12.3–12.7	4.83	9.1	1 pinning H_2O/Keggin
AMT-0	12.3	5.10	8.7	0 pinning H_2O/Keggin, Keggin alignment varied

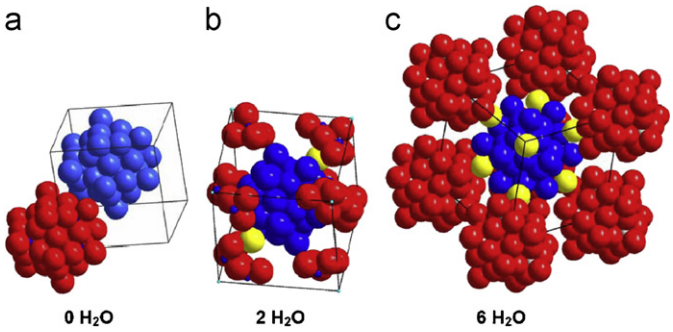

Fig. 9. Simulated crystal structures with pinning structural water: (a) AMT-0 (dehydrated), (b) AMT2–6 (two structural waters), (c) AMT20–22 (six structural waters).

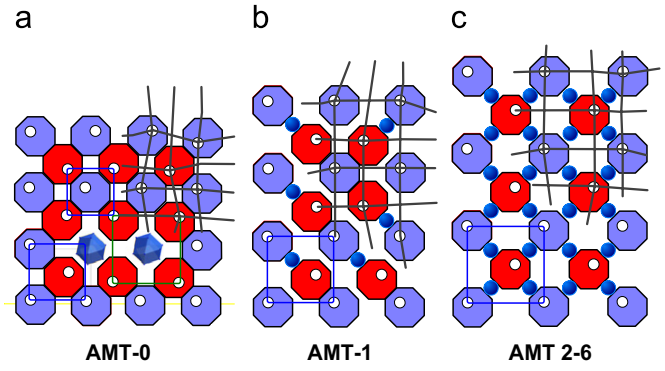

Fig. 10. Schematic representation of cubic structural disorder. In two dimensions, octagons represent the 3-D space allotment for a given molecule, where white circles show the scattering center of the molecule positioned within the space allotment of the structure. Lines show the localized unit cell: (a) disorder from molecular rotation during consolidation, showing three apparent unit cell sizes as squares, (b) disorder from pinning structural water (blue circles) and molecule rotation, (c) fully hydrated, the structure can exhibit larger displacements. In each drawing, the lower left corner shows the highest order and the upper right the least.

hollow sites. Fig. 11b shows Pt atoms on a 111 face, spaced at 2.774 Å. Fig. 11c shows the spacing for unreduced metatungstate ion, where W–W is 3.315 Å. Fig. 11d shows the electroreduced metatungstate spacing at 2.501 Å [14], showing a spacing that is within 10% of the spacing for Pt, and helps to account for the observed electrocatalytic activity. The metal–metal distance of 2.5 Å moves the reduced metatungstate into a metal–metal bonding regime. In this regime, electrons could be shuttled quickly for catalytic transitions. Also, activated metatungstate sites would contain three edge atoms, as opposed to multi-atomic platinum metal surfaces, where adsorbates are known to "walk" to edge atoms before catalytic conversion. The small metal-ensemble size may also explain the catalyst's tolerance to CO during catalyst testing [5].

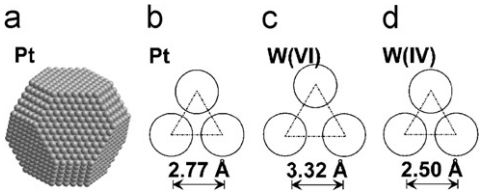

Fig. 11. Comparison of platinum and metatungstate active sites: (a) typical Pt nanocrystal, (b) Pt 111 atomic spacing is 2.77 Å, (c) unreduced metatungstate W–W spacing is 3.32 Å, (d) reduced metatungstate W–W spacing moves to 2.50 Å [14], and is catalytically active [5].

For a commercially viable catalyst, a minimum power density is required. This is often estimated using *site density* and *turnover rate*. With equal site densities, the turnover rate could be 10 × slower than Pt and still provide a minimum acceptable power density for commercialization [21]. Working from the model idealized in Fig. 11a, a Pt nanocrystal on a graphite support would have 72 edge atoms. A similarly sized AMT crystal on graphite would have 82 exposed W–W–W face sites. This provides a first approximation of structural feasibility for application as a fuel cell catalyst.

4.4. Summary

The long-term order as a mixture of *distorted cubic* structures is supported by various experimental and modeled means. The distorted cubic structure is a framework to locate the Keggin anions in a statistical ensemble with a generally eutactic-BCC arrangement. In this way, the single broad initial powder diffraction peak of AMT-0 at 8.7 Å represents the "Gaussian-normal curve" of positional variation within the arrangement. Non-symmetry is caused by lattice strain from hydrogen bonded water, rotational geometry, and water motion. Powders appear to be a mixture of crystals with slightly different sized lattice parameters. The building blocks, as shown by TEM-ED, fit into the structural scheme for the forms AMT-0 and AMT-1, with bulk samples containing a complex mixture of lattice sizes and orientations. Density measurements and XRD data support a unit cell growth due to structural hydration to the stable form AMT-4. For AMT-0, a cell volume of 929 Å^3/Keggin represents the highest documented packing density of metatungstate ions.

Acknowledgments

Special thanks to Mr. Jeffrey N. Dann for extensive powder XRD testing, also to Mr. Ronald E. Rockwell and Mr. Harry O. Fassett for XRD testing. Thanks to Mr. Henry H. Eichelberger for TEM and TEM-ED work. Also thanks to Dr. Peter J. Zavalij for single-crystal X-ray work and discussions, Dr. David M. Jenkins for furnace-XRD testing, Mr. John E. Miller for density measurements, Dr. Alan Benesi for ^{183}W NMR work, and to Dr. Sean P.E. Smith and

Dr. Shailesh Upreti for discussions. Thanks to the staff at the Cornell High Energy Synchrotron Source, especially Dr. Ken Finkelstein, Dr. Zongwu Wang, and also to Dr. Qxiun Guo of Los Alamos National Laboratory, and Dr. Héctor Abruña of Cornell University.

References

[1] V.M. Akhmedov, S.H. Al-Khowaiter, Catal. Rev. 49 (2007) 33–139.
[2] M.H. Zhang, H.H. Hwu, M.T. Buelow, J.G.G. Chen, T.H. Ballinger, P.J. Andersen, Catal. Lett. 77 (1-3) (2001) 29–34.
[3] J.B. Christian, R.G. Mendenhall, US Patent 6,656,870, 2003.
[4] J.B. Christian, R.G. Mendenhall, US Patent 7,060,648, 2006.
[5] J.B. Christian, S.P.E. Smith, M.S. Whittingham, H.D. Abruña, Electrochem. Commun. 9 (2007) 2128.
[6] S.P.E. Smith, J.B. Christian, Electrochem. Acta 53 (2008) 2994.
[7] P.N. Ross Jr., in: W. Vielstich, H.A. Gasteiger, A. Lamm (Eds.), Handbook of Fuel Cells, vol. 2, Wiley, New York, 2003 (Chapter 31).
[8] R.W. Mooney, V. Chiola, C.W.W. Hoffman, C.D. Vanderpool, J. Electrochem. Soc. 109 (1962) 1179.
[9] ICDD-JCPDS Powder Diffraction File #00-039-0186.
[10] M.T. Pope, G. Varga, Inorg. Chem. 5 (1964) 1249.
[11] S.-Y. Mao, X.-X. Ren, X.-X. Liu, J.-X. Mi, Acta Crystallogr. E 62 (2006) i187.
[12] J.C.A. Boeyens, G.J. McDougall, J. Van R. Smit, J. Solid State Chem. 18 (1976) 191–199.
[13] J.F. Keggin, Proc. R. Soc. London Ser. A 144 (1934) 75.
[14] Y. Jeannin, J.-P. Launay, M.A.S. Sedjadi, Inorg. Chem. 19 (1980) 2933.
[15] T. Yamase, E. Ishikawa, J. Chem. Soc. Dalton Trans. (1996) 1619.
[16] C. Boskovic, M. Sadek, R.T.C. Brownlee, A.M. Bond, A.G. Wedd, J. Chem. Soc. Dalton Trans. 2001 (2001) 187.
[17] H. Putz, J.C. Schon, M. James, J. Appl. Crystallogr. 32 (1999) 864–870.
[18] K.W. Andrews, D.J. Dyson, S.R. Keown, Interpretation of Electron Diffraction Patterns, second ed, Plenum Press, New York, 1971.
[19] A. Le Bail, Powder Diffr. 19 (2004) 249–254.
[20] (a) M.S. Dresselhaus, G. Dresselhaus, P.C. Eklund, Science of Fullerenes and Carbon Nanotubes, Academic Press, New York, 1996;
(b) B.K. Vainshtein, V.M. Fridkin, V.L. Indenbom, Structure of Crystals, third ed, Springer, Berlin, 2000;
(c) C. Laforge, D. Passerone, A.B. Harris, P. Lambin, E. Tosatti, Phys. Rev. Lett. 87 (2001) 085503;
(d) Z. Belahmer, P. Bernier, L. Firlej, J.M. Lambert, M. Ribet, Phys. Rev. B 47 (1993) 15980–15983;
(e) J. Wu, M. Gu, D.W. Liu, S.S.K. Keung, T.B. Tang, J. Appl. Phys. 95 (2004) 4093–4095;
(f) Y. Kita, K. Wako, H. Goto, T. Naito, H. Kawai, I. Okada, J. Chem. Phys. 125 (2006) 034506.
[21] H.A. Gasteiger, S.S. Kocha, B. Sompalli, F.T. Wagner, Appl. Catal. B 56 (2005) 9–35.
[22] H. Weiner, H.-J. Lunk, R. Friese, H. Hartl, Inorg. Chem. 44 (2005) 7751–7761.
[23] P. Zavalij, J. Guo, M.S. Whittingham, R.A. Jacobson, V. Pecharsky, C.K. Bucher, S.-J. Hwu, J. Solid State Chem. 123 (1996) 83–92.
[24] M. Asami, H. Ichida, Y. Sasaki, Acta Crystallogr. C 40 (1984) 35–37.
[25] J.-C.P. Gabriel, R. Nagarajan, S. Natarajan, A.K. Cheetham, C.N.R. Rao, J. Solid State Chem. 129 (1997) 257.
[26] U. Lee, H.-C. Joo, K.-M. Park, T. Ozeki, Acta Crystallogr. C 59 (2003) m152–m155.
[27] Q.-X. Han, J.-P. Wang, L.-H. Song, Acta Crystallogr. E 62 (2006) i201–i203.